Efficient broadband frequency conversion via simultaneous adiabatic three wave mixing processes

Gil Porat and Ady Arie

Citation: Appl. Phys. Lett. **102**, 151108 (2013); doi: 10.1063/1.4802597
View online: http://dx.doi.org/10.1063/1.4802597
View Table of Contents: http://apl.aip.org/resource/1/APPLAB/v102/i15
Published by the American Institute of Physics.

Efficient broadband frequency conversion via simultaneous adiabatic three wave mixing processes

Gil Porat and Ady Arie
Department of Physical Electronics, Tel Aviv University, Tel Aviv 69978, Israel

(Received 21 November 2012; accepted 7 April 2013; published online 18 April 2013)

Two frequency-cascaded and spatially simultaneous three-wave-mixing processes, each pumped by a different frequency, are studied in a quasi-phase-matching crystal with chirped poling. Theory, numerical simulation, and experiment all show that efficient two-process adiabatic frequency conversion takes place over a broad range of input wavelengths. Experimentally, up to five process cascades are obtained. Furthermore, it is demonstrated that reversing the chirp sign results in a different conversion for the same input wavelength. This method can be applied to generation of an all-optically tunable frequency comb. © *2013 AIP Publishing LLC* [http://dx.doi.org/10.1063/1.4802597]

Three wave mixing (TWM) processes in quadratic nonlinear crystals are widely exploited for optical frequency conversion.[1] Such processes are utilized to generate laser frequencies that are not available directly from laser action. By combining two TWM processes, frequency conversion between near or far frequencies can also be obtained.[2] In order for a TWM process to be efficient, a phase-matching condition has to be satisfied.[1] This can be achieved by quasi phase matching (QPM), in which the sign of the nonlinear coefficient of a ferroelectric crystal is modulated along the crystal.[3] For a single process, QPM is easily provided, while simultaneous QPM of multiple processes remains a challenge, and comes at the expense of conversion efficiency.[2,3]

Recently, an analogy between TWM processes and interaction of few-state atoms with electromagnetic (EM) fields has been utilized to obtain favorable properties for frequency conversion.[4–10] Suchowski *et al.* and Moses *et al.* demonstrated efficient and broadband sum frequency generation (SFG)[4,5] and difference frequency generation (DFG).[6] The increase in efficiency and bandwidth was attributed to the use of an adiabatically chirped QPM grating, which mimics the atomic process of rapid adiabatic passage.[11] In other works,[7,8] various QPM architectures were suggested as analogies of atomic adiabatic elimination[11] or stimulated Raman adiabatic passage.[11] In these schemes, two frequency-cascaded TWM processes take place simultaneously, with fixed or controllably varying efficiencies along the interaction, and generate a new frequency without an intermediate one. In yet another publication,[10] Rangelov *et al.* theoretically demonstrated that efficient and broadband conversion can be performed via two spatially simultaneous and frequency-cascaded SFG processes in an adiabatically chirped QPM grating, with one pump for both processes.

In this letter, efficient and broadband frequency conversion is demonstrated experimentally, where frequency-cascaded SFG and DFG processes are performed simultaneously, pumped by two separate laser frequencies, reaching up to a five-process cascade. Furthermore, theory and experiment show that reversal of the chirp sign results in a different conversion process for the same input wavelength.

Four processes are considered here (see insets of Fig. 1). Two of them are upconversion of ω_1 with each pump, $\omega_1+\omega_{p_1}=\omega_{2a}$ and $\omega_1+\omega_{p_2}=\omega_{2b}$, and two processes are downconversion of the generated waves: $\omega_{2a}-\omega_{p_2}=\omega_{3a}$ and $\omega_{2b}-\omega_{p_1}=\omega_{3b}$. ω_1,ω_{p_1} and ω_{p_2} are the input, first pump and second pump frequency, respectively, where we choose $\omega_{p_1}>\omega_{p_2}$ without loss of generality. We then have $\omega_{3a}=\omega_1+\omega_{p_1}-\omega_{p_2}>\omega_1>\omega_{3b}=\omega_1+\omega_{p_2}-\omega_{p_1}$, so conversion of ω_1 to ω_{3a} (ω_{3b}) is upconversion (downconversion). We work in the rotating frame defined by $A_j(z)=\tilde{A}_j exp[if_j(z)z]$, where $f_1(z)=-\Delta k_1(z)$, $f_{2a}(z)=0$, $f_{3a}(z)=-\Delta k_2(z)$, $f_{2b}(z)=\Delta k_3(z)-\Delta k_1(z)$, $f_{3b}(z)=\Delta k_3(z)-\Delta k_1(z)-\Delta k_4(z)$. $\tilde{A}_j$ is the complex amplitude of the field with frequency ω_j, and $\Delta k_j(z)$ is the phase-mismatch of the j-th process. For a linearly chirped crystal, we use the approximate relation $\Delta k_j(z)=\Delta k'_j+\frac{2\pi}{\Lambda(z)}$, where $\Lambda(z)$ is the local QPM modulation period, and $\Delta k'_j$ is the dispersion phase mismatch of the j-th process, i.e., $\Delta k'_1=k_1+k_{p1}-k_{2a}$, $\Delta k'_2=k_{p2}+k_{3a}-k_{2a}$, $\Delta k'_3=k_1+k_{p2}-k_{2b}$, and $\Delta k'_4=k_{p1}+k_{3b}-k_{2b}$. Using the plane-wave and constant pump approximations, the coupled wave equations for this system are $d\psi/dz=iM(z)\psi(z)$, where $\psi(z)=[A_1\ A_{2a}\ A_{3a}\ A_{2b}\ A_{3b}]^T$ is the amplitudes vector and

$$M=\begin{bmatrix}\Delta k_1 & \kappa_{1,2a} & 0 & \kappa_{1,2b} & 0\\ \kappa_{2a,1} & 0 & \kappa_{2a,3a} & 0 & 0\\ 0 & \kappa_{3a,2a} & \Delta k_2 & 0 & 0\\ \kappa_{2b,1} & 0 & 0 & \Delta k_1-\Delta k_3 & \kappa_{2b,3b}\\ 0 & 0 & 0 & \kappa_{3b,2b} & \Delta k_1+\Delta k_4-\Delta k_3\end{bmatrix} \quad (1)$$

is the coupling matrix. Here $\kappa_{1,2a}=A^*_{p_1}\chi^{(2)}\omega_1^2/k_1c^2$, $\kappa_{1,2b}=A^*_{p_2}\chi^{(2)}\omega_1^2/k_1c^2$, $\kappa_{2a,3a}=\tilde{A}_{p_2}\chi^{(2)}\omega_{2a}^2/k_{2a}c^2$, and $\kappa_{2b,3b}=\tilde{A}_{p_1}\chi^{(2)}\omega_{2b}^2/k_{2b}c^2$, where $\kappa_{ij}=(\omega_i^2k_j/\omega_j^2k_i)\kappa^*_{ji}$, are the effective coupling coefficients. $\chi^{(2)}$ is the second-order nonlinear coefficient of the crystal, c is the speed of light, and $k_j=n_j(\omega_j)\omega_j/c$ is the wavenumber of the wave with frequency ω_j. The remainder of the analysis will be performed by studying the eigenvalues of the coupling matrix M, using arbitrary parameter values chosen for the sake of clarity. This approach will lead to an analogy with avoided crossings of EM coupled electronic eigenstates in atoms or molecules.[11]

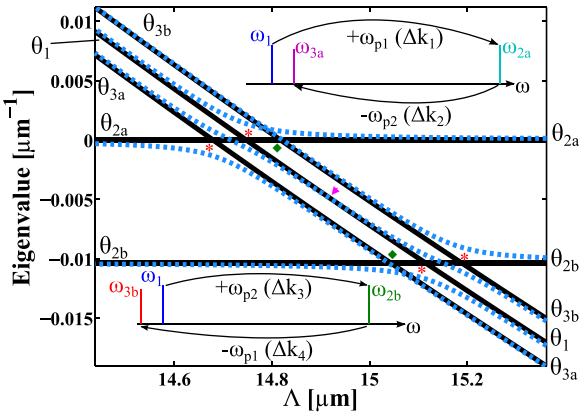

FIG. 1. Eigenvalues of the coupling matrix M in the absence of coupling (solid black lines) and with nonzero coupling (dash blue lines). Each inset shows one cascade on the frequency axis.

First, note that when there is no coupling, i.e., $\kappa_{i,j} = 0$ for all i and j, the matrix is diagonal. This means that each wave evolves as $A_j(z) = A_j(0)exp(i\theta_j z)$, where θ_j is its eigenvalue, and if all but one of the amplitudes are nonzero, then the system is in a stationary state. In Fig. 1, the eigenvalues in the absence of coupling are plotted vs. the local QPM period in black solid lines. The eigenvalues of the two upconverted waves (θ_{2a} and θ_{2b}) are independent of the QPM period, whereas the eigenvalues of the input wave θ_1 and the two-process products θ_{3a} and θ_{3b} are inversely proportional to the QPM period. At each crossing of two of these black solid lines $\theta_i = \theta_j$ for some pair of i and j. Since θ_j determines the phase for A_j, $\theta_i = \theta_j$ means that the total phase difference between A_i and A_j is zero, i.e., if these two waves can be coupled by a TWM process, it would be phase-matched at this point. The phase-matching points of the four TWM processes considered here correspond to the crossings that are marked with red asterisks. The two additional crossings, marked with green diamonds, correspond to three-photon adiabatic elimination processes.[7] Due to their inherently low efficiency as compared to phase-matched TWM processes, they are neglected here.

The eigenvalues in the presence of coupling are plotted in Fig. 1 as dashed blue lines. Note that the eigenvalues in the absence of coupling (solid black lines in Fig. 1) depend only on the material dispersion and the QPM period, whereas when coupling is present, the dashed blue lines bend. They bend such that the crossings are avoided, where greater pump intensity leads to greater bending. Far from crossings, the dashed and solid lines are near. The physical interpretation of this graphical phenomenon is that, due to the coupling, energy in a single frequency is no longer a stationary state of the system near crossings (i.e., phase-matching). If such a state is obtained near a crossing, energy will be transferred from one frequency to another as light propagates along the z axis. This is another way of explaining how phase-matching increases the amount of energy being transferred between two frequencies. The actual stationary states of the system are the ones that correspond to the eigenvalues along the dashed blue lines.

According to adiabatic theorem,[11] a system placed in a stationary state and experiences only adiabatic changes will remain in the same stationary state throughout its evolution. For a TWM process with phase-mismatch Δk and coupling coefficient κ, it is sufficient that $|d\Delta k/dz| \lesssim |\kappa|$ at the crossing in order for a QPM chirp rate to be considered adiabatic.[4,5,10] Such adiabatic evolution can be described graphically: if the system is "on" one of the dashed blue lines in Fig. 1, and the crystal is chirped adiabatically with increasing period, then the system will follow the same dashed line, going from left to right, as light propagates along the crystal. For example, consider the case where the crystal is chirped from $\Lambda = 14.9\,\mu$m to $\Lambda = 15.4\,\mu$m, and only the ω_1 wave enters the crystal along with the two pumps. Starting at the point marked by the purple arrow in the center of Fig. 1, the system will then follow the dashed blue line from left to right, until it converges with the solid line of θ_{3b}. We conclude that energy will be efficiently transferred from ω_1 to ω_{3b}, resulting in downconversion. We note that this path also crosses the solid line of θ_{2b}, so we expect the energy to go through ω_{2b} on its way from ω_1 to ω_{3b}. This can be viewed as two cascaded adiabatic processes, $\omega_1 \rightarrow \omega_{2b}$ and $\omega_{2b} \rightarrow \omega_{3b}$. Conversely, if the crystal was chirped from $\Lambda = 15.4\,\mu$m to $\Lambda = 14.9\,\mu$m, then the system would start at the dashed blue line near θ_1 at the bottom right of Fig. 1, and follow this line to the left, corresponding to upconversion of ω_1 to ω_{2b}. Hence, for the same input wave, a different frequency will be generated, depending on whether the chirp is positive or negative. Finally, note that changing the input frequency ω_1 results in horizontal translation of the eigenvalues plot (vertical translation is avoided by our choice of the rotating frame, which is defined such that $\theta_{2a} = 0$). As long as the shift is such that all of the crossings are still within the chirp range of the crystal, the same arguments can be applied. The same chirped crystal can thus facilitate these processes for a wide range of input frequencies.

Numerical simulations were conducted in order to verify the theoretical predictions. In the simulations, Nd:YLF ($\lambda_{p_1} = 1047.5$ nm) and Nd:YAG ($\lambda_{p_2} = 1064.5$ nm) lasers were used as pumps, with $I_{p_1} = I_{p_2} = 50\,\mathrm{MW/cm^2}$. The nonlinear medium was a 35 mm long $KTiOPO_4$ crystal, with $\chi^{(2)} = 32$ pm/V (Ref. 12) and QPM period linearly chirped from $\Lambda = 14.38\,\mu$m to $\Lambda = 14.92\,\mu$m, kept at a temperature of 100 °C. Sellmeier equations[13,14] were used to account for dispersion.

The simulations reveal four different scenarios of efficient adiabatic frequency conversion, where each corresponds to a different path in the eigenvalues plot. The difference between the four cases is the chirp sign and the input wavelength. As examples, input wavelengths of 1509 nm and 1542 nm were used in the simulations presented in Figs. 2 and 3.

For the first case, a positive chirp was used with an input wavelength of $\lambda_1 = 1509$ nm. The resulting intensities, normalized to the input intensity, are displayed in Fig. 2(a), with the corresponding eigenvalues plot in Fig. 2(b). Fig. 2(a) shows that energy is efficiently downconverted from $\lambda_1 = 1509$ nm to $\lambda_{3b} = 1544.5$ nm through $\lambda_{2b} = 624.2$ nm. (The $\lambda_1/\lambda_{2b} = 2.42$ photon energy ratio is the reason that the normalized peak intensity at $\lambda_{2b} = 624.2$ nm is greater than 1. The additional energy comes from the second pump). This corresponds to the picture revealed in Fig. 2(b), where the system follows the dashed line marked with arrows, which goes from θ_1 to θ_{3b} through θ_{2b}. The inset of Fig. 2(a) shows

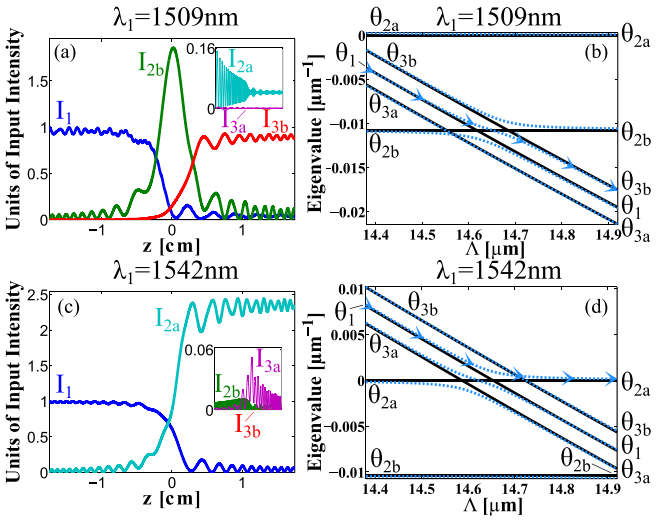

FIG. 2. Numerically obtained intensities along a positively chirped crystal (insets have the same horizontal axis as figures). The adiabatic interactions in (a) and (c) follow the paths marked with arrows in the coupling matrix eigenvalues plots in (b) and (d), respectively. $\lambda_1 = 1509$ nm is (a) and (b). $\lambda_1 = 1542$ nm is (c) and (d).

that some energy was transferred to $\lambda_{2a} = 618.3$ nm due to non-adiabatic coupling. This is a result of the non-ideal dynamics, i.e., the system does not perfectly follow the ideal path, which would require an infinitely slow chirp rate.

In the second case, the period was also positively chirped, but the input wavelength was $\lambda_1 = 1542$ nm. Fig. 2(c) shows that in this case the input energy is transferred to $\lambda_{2a} = 618.3$ nm, where the inset displays relatively low non-adiabatic conversion to other wavelengths. Once again, the eigenvalues plot, shown in Fig. 2(d), describes the same scenario, where the path the system ideally follows goes from θ_1 to θ_{2a}.

For the third and fourth cases, the same two input wavelengths were used, but this time the QPM period was negatively chirped. The results, displayed in Fig. 3, show the same behavior and correspondence with the eigenvalue representation as those obtained with the positive chirp. However, with the negative chirp, the energy at $\lambda_1 = 1509$ nm was transferred to $\lambda_{2b} = 624.2$ nm, while $\lambda_1 = 1542$ nm was upconverted to

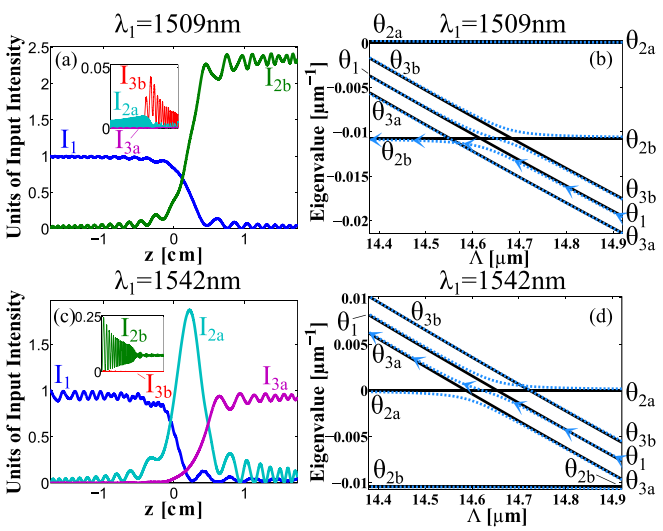

FIG. 3. Same as Fig. 2 for a negatively chirped crystal.

$\lambda_{3a} = 1475.1$ nm. This is in contrast to previously considered adiabatic interactions in chirped crystals, where either the chirp sign did not affect the outcome, or that upon reversal of the chirp sign, the same conversion would take place through a different adiabatic path.[4,5,10]

As mentioned above, 1509 nm and 1542 nm were each an example of the characteristics of some input wavelength interval. The extent of these intervals is revealed in Figs. 4(a) and 4(b), which display the normalized output intensities vs. the input wavelength for positive and negative chirp, respectively. The four cases are distinct in these figures: the first case ($\lambda_1 \rightarrow \lambda_{3b}$) takes place over a 30 nm full width at half maximum (FWHM) band around 1505 nm, while the second case ($\lambda_1 \rightarrow \lambda_{2a}$) spans the interval from 1520 nm to 1564 nm, both seen in Fig. 4(a). In Fig. 4(b), the third case ($\lambda_1 \rightarrow \lambda_{2b}$) is obtained for $1490\,\text{nm} < \lambda_1 < 1534\,\text{nm}$, and the fourth case ($\lambda_1 \rightarrow \lambda_{3a}$) has a 32 nm FWHM bandwidth around 1549 nm. Clearly, reversing the sign of the chirp drastically changes the interaction for any input wavelength over a 75 nm interval.

These theoretical predictions were tested experimentally, using the same chirped $KTiOPO_4$ crystal as in the simulation. The experimental conditions were similar to the ones used in simulation, however due to technical constraints they were not identical. First, the beam radii in the experiment were $\sim$55 μm for each pump beam and $\sim$100 μm for the input beam. The Rayleigh range for all three beams was approximately 16 mm in the crystal. Second, the two actively Q-switched pump lasers used in the experiment had pulse durations of $\tau_{p_1} \sim 13.5$ ns and $\tau_{p_2} \sim 4.5$ ns. Correspondingly, the peak pumps intensities inside the uncoated crystal were $I_{p_1} \sim 6\,\text{MW/cm}^2$ and $I_{p_2} \sim 105\,\text{MW/cm}^2$, where Fresnel reflections were taken into account. The input wave was generated by an optical parametric oscillator (OPO), pumped by the Nd:YAG laser, and had a similar pulse duration to that of the Nd:YAG. The OPO produced a distorted Gaussian beam, with peak intensity of $\sim$1.6 MW/cm^2. The pulses of the two 10 kHz Q-switched lasers were synchronized by a delay generator that fed electrical signals to their acousto-optic modulators. In practice, the temporal difference between the peaks of two pulses randomly varied by as much as tens of nanoseconds. Each experimental result here is an average of 10 measurements, where each measurement had an integration time of 1 ms, so each result represents an averaging over 100 laser pulses, normalized according to the input power. These results take background noise and Fresnel reflections into consideration, such that they represent internal conversion efficiency.

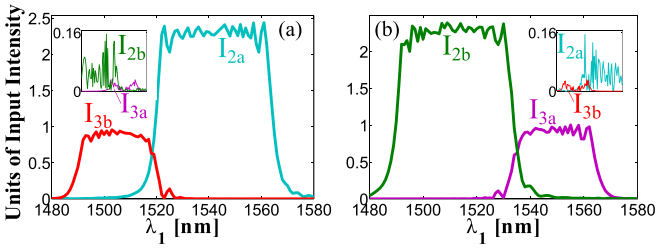

FIG. 4. Numerical results of output intensity vs. input wavelength for (a) positive chirp and (b) negative chirp (insets have the same horizontal axis as figures).

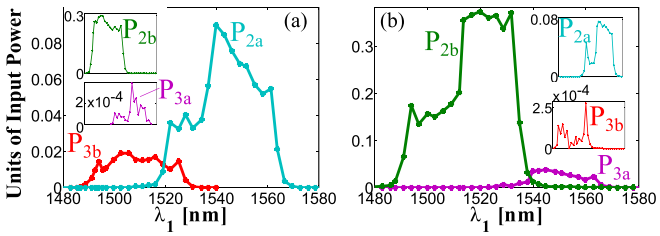

FIG. 5. Experimental results of output power vs. input wavelength for (a) positive chirp and (b) negative chirp (insets have the same horizontal axis as figures).

The experimental results contain all the salient features of theory and simulation, despite the low intensity of the Nd:YLF pump laser and the partial spatial and temporal overlap of the beams and pulses, which limit the experimental two-process conversion efficiency to 3.77% at most. Figs. 5(a) and 5(b) show the normalized output power experimentally obtained for positive and negative chirp, respectively. The top inset of Figs. 5(a) and 5(b) reveals that when the input λ_1 was converted to λ_{3b} (λ_{3a}) through λ_{2b} (λ_{2a}), a significant amount of energy remained in the intermediate wavelength at the end of the interaction. This is a result of the low pump intensity, graphically manifested as a reduced bending of the dashed lines. The bottom insets of Figs. 5(a) and 5(b) show low power resulting from weak non-adiabatic coupling, in correspondence to the simulation results (see insets of Figs. 4(a) and 4(b)).

In the experiment, for a certain range of input wavelengths, the product of the two-process conversion was itself converted. The reason was that the acceptance bandwidth of the two-process conversion was greater than the difference between the frequencies of the two pump lasers, so the product was inside the acceptance bandwidth of the same two-process conversion. For example, for positive period chirp, the product ω_{3b} can participate in the SFG process $\omega_{3b} + \omega_{p_2} = \omega_{4b}$, followed by the DFG process $\omega_{4b} - \omega_{p_1} = \omega_{5b}$. Fig. 6 shows the optical spectrum analyzer measurement for this case, where $\lambda_1 = 1489\,\text{nm}$, $\lambda_{3b} = 1523.6\,\text{nm}$ and $\lambda_{5b} = 1559.8\,\text{nm}$. The same was observed for $1488.7 \le \lambda_1 \le 1496.9\,\text{nm}$, with normalize power up to 5×10^{-4}. Furthermore, λ_{5b} is within the acceptance bandwidth of the adiabatic SFG process with the first pump (see Fig. 4(a)), i.e., $\omega_{5b} + \omega_{p1} = \omega_{6a}$. This product was also observed in the experiment, with a peak normalized power of 1.7×10^{-2}. A similar argument holds for negative chirp, where we have $\omega_{3a} + \omega_{p_1} = \omega_{4a}$, followed by $\omega_{4a} - \omega_{p_2} = \omega_{5a}$ and then $\omega_{5a} + \omega_{p2} = \omega_{6b}$. These processes were observed experimentally as well, with peak normalized powers of 5.4×10^{-4} and 3.8×10^{-3} for λ_{5a} and λ_{6b}, respectively. Note that, overall, five frequency-cascaded processes were performed simultaneously.

These multiple frequency-cascaded processes suggest an interesting application: an all-optically tunable frequency comb. The pump frequencies should be chosen such that the difference between them is much smaller than the two-process conversion bandwidth. There will then be many cascades of conversion, since each cascade-product will still be within the acceptance bandwidth of the same process that generated it. The spectral spacing between these products would be equal to the spectral spacing between the two pumps. In this manner a frequency comb can be obtained, where the central frequency and teeth spacing can be all-optically tuned by tuning the frequencies of the input and pumps. High efficiency for many cascades can be obtained by placing the chirped crystal in a resonator, or using CW lasers with a fiber-coupled chirped QPM waveguide[3] in a fiber loop. Note also that energy that remains in an intermediate wavelength after one pass through the crystal will get converted to one of the comb "teeth" in the next pass. For example, see the $\theta_{2a} \rightarrow \theta_{3a}$ path that goes from left to right on the dashed blue line of Fig. 2(d).

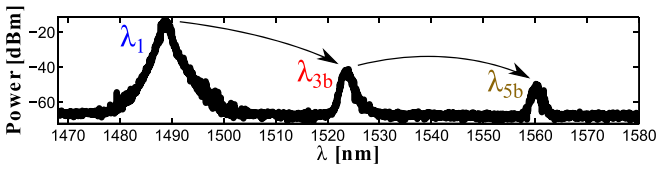

FIG. 6. Optical spectrum analyzer measurement showing multiple adiabatic conversions.

In conclusion, multiple-process broadband adiabatic frequency conversion has been demonstrated theoretically and experimentally. Up to five frequency-cascaded processes were demonstrated by experiment. Furthermore, a chirped-crystal system was experimentally shown to perform different conversion for the same input wavelength, depending on the chirp sign. Finally, it was explained how the same method can be used to generate all-optically tunable frequency combs.

[1]R. W. Boyd, *Nonlinear Optics*, 3rd ed. (Academic Press, Waltham, MA, 2008).
[2]S. M. Saltiel, A. A. Sukhorukov, and Y. S. Kivshar, Prog. Opt. **47**, 1–73 (2005).
[3]D. S. Hum and M. M. Fejer, C. R. Phys. **8**, 180–198 (2007).
[4]H. Suchowski, D. Oron, A. Arie, and Y. Silberberg, Phys. Rev. A **78**, 063821 (2008).
[5]H. Suchowski, V. Prabhudesai, D. Oron, and Y. Silberberg, Opt. Express **17**, 12731–12740 (2009).
[6]J. Moses, H. Suchowski, and F. X. Krtner, Opt. Lett. **37**, 1589–1591 (2012).
[7]G. Porat, Y. Silberberg, A. Arie, and H. Suchowski, Opt. Express **20**, 3613–3619 (2012).
[8]G. Porat and A. Arie, J. Opt. Soc. Am. B **29**, 2901–2909 (2012).
[9]S. Longhi, Opt. Lett. **32**, 1791–1793 (2007).
[10]A. A. Rangelov and N. V. Vitanov, Phys. Rev. A **85**, 045804 (2012).
[11]D. Tannor, *Introduction to Quantum Mechanics: A Time-Dependent Perspective* (University Science Books, Sausalito, CA, 2007).
[12]D. N. Nikogosyan, *Nonlinear Optical Crystals* (Springer, New York, NY, 2005).
[13]K. Fradkin, A. Arie, A. Skliar, and G. Rosenman, Appl. Phys. Lett. **74**, 914–916 (1999).
[14]S. Emanueli and A. Arie, Appl. Opt. **42**, 6661–6665 (2003).